

Operando impedance spectroscopy with combined dynamic measurements and overvoltage analysis in lithium metal batteries

Received: 9 September 2024

Accepted: 14 February 2025

Published online: 27 February 2025

 Check for updatesSara Drvarič Talian ¹, Gregor Kapun ¹, Jože Moškon ¹,
Robert Dominko ^{1,2,3} & Miran Gabersček ^{1,2} 

State-of-the-art battery cells are composed of complex heterogeneous electrode structures that pose significant challenges for analyzing electrochemical processes. Traditional electrochemical impedance spectroscopy (EIS) techniques require system simplification and equilibrium conditions, which limit their ability to capture dynamic processes during battery operation. This paper introduces an advanced method, which combines *operando* impedance measurements with real-time monitoring of overvoltage in a three-electrode cell setup. This approach enables detailed analysis of processes occurring under actual operating conditions, overcoming limitations of conventional EIS. The benefits of *operando* EIS are demonstrated through the study of lithium-metal electrodes during repetitive stripping and plating cycles. The technique allows for the identification and quantification of various electrochemical processes, including those related to lithium diffusion, surface morphology changes, and dendritic growth. The findings highlight the importance of *operando* impedance spectroscopy in providing insights that are not accessible through traditional EIS methods, particularly in understanding complex phenomena such as internal short circuits and lithium pitting. The study emphasizes the necessity of combining *operando* impedance measurements with equilibrium measurements to achieve a comprehensive understanding of battery behavior during operation.

State-of-the-art battery cells consist of complex electrodes composed of several different materials that form complicated heterogeneous structures in the nanometer to micrometer range. The identification and quantitative evaluation of the processes taking place in such electrodes is in principle possible by electrochemical measurements using electrochemical impedance spectroscopy (EIS)^{1–3}. The first step in analyzing electrode processes is usually a system simplification

(Fig. 1a), where the cell and electrode design are simplified to reduce the number of variables. This could mean, for example, preparing flat instead of porous electrodes and a symmetrical cell assembly^{4–7}. Then the impedance spectroscopy is measured at equilibrium (Fig. 1b). This is because EIS measurements require that the system under investigation is linear, stable, causal and stationary (i.e. time-invariant)⁸. In the case of batteries, all these conditions can usually only be met after a

¹Department of Materials Chemistry, National Institute of Chemistry, Hajdrihova 19, 1000 Ljubljana, Slovenia. ²Faculty of Chemistry and Chemical Technology, University of Ljubljana, Večna pot 113, 1000 Ljubljana, Slovenia. ³ALISTORE - European Research Institute, CNRS FR 3104, 15 Rue Baudelocque, Amiens 80039 Cedex, France. ✉ e-mail: miran.gaberscek@ki.si

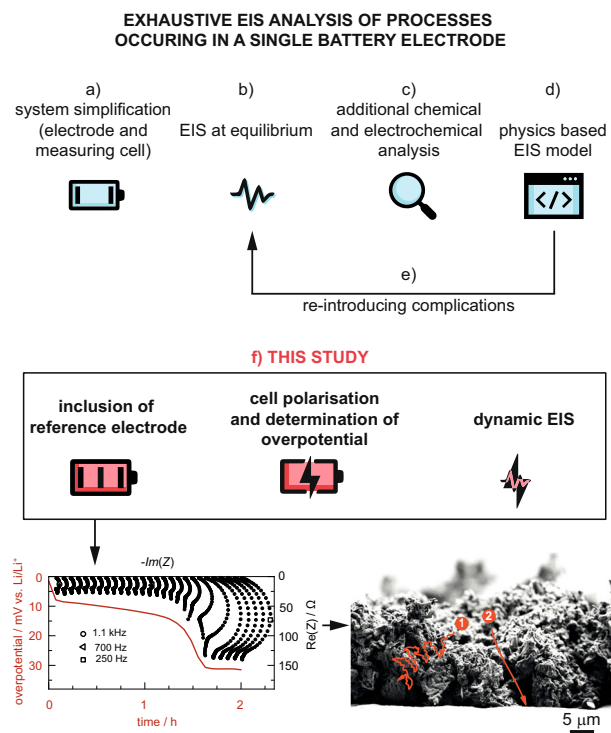


Fig. 1 | Schematic representation of EIS analysis. a–e Traditional steps in EIS analysis in battery research **(f)** approach in this study.

sufficient rest period at open circuit voltage (when no current is flowing through the system), or alternatively, after the voltage of the cell has been kept constant and the current has dropped sufficiently. Therefore, if we want to study the changes that occur during the discharge (or charge) half-cycle of a battery using EIS, specific protocols must be followed as described in Supplementary Note 1.

After reliable measurements of impedance spectra, the EIS analysis must be supported by additional electrochemical, chemical and morphological analyzes (Fig. 1c), which then enable the construction of the proposed physics-based EIS model (Fig. 1d). The entire workflow is repeated by gradually introducing complications that were originally omitted in order to understand the elementary processes in the actual complex battery electrode (Fig. 1e). Despite its reliability and general usefulness, the described protocol has one major drawback: it only provides information about what happens in the battery after equilibrium is reached, while it lacks the crucial information about the nature of the processes that take place under the actual operating conditions of the battery. In principle, this information can be collected with the help of so-called dynamic impedance measurements⁹ (Supplementary Note 2 and Fig. S1).

Dynamic electrochemical impedance spectroscopy (DEIS), also known as galvanostatic electrochemical impedance spectroscopy (GEIS), or *operando* EIS was first applied to various battery systems back in the early 1990s, as a technique then referred to as non-stationary or in-situ impedance spectroscopy. Studies ranged from the analysis of lead-acid batteries¹⁰ to the deposition and dissolution of lithium¹¹, the operation of graphite electrodes¹², the formation of LiCoO₂ interfaces¹³ and the determination of the deintercalation and intercalation of lithium in three-electrode Li-ion batteries¹⁴. More recently, Huang et al. used dynamic single-frequency measurements over the entire SOC range of a commercially available 18650 cell, which showed differences in charge transfer resistance and a dramatic increase in impedance near full discharge¹⁵. Ko et al. used this technique to investigate the differences between mm- and nm- sized particles in silicon anodes¹⁶. Ratynski et al. used the direct current

superimposed EIS measurements to determine changes in active surface area in Li-ion battery electrodes¹⁷. Watanabe et al. showed hysteresis and particle size of active material on charge transfer resistance¹⁸, while Brown et al. used the technique to detect the onset of lithium plating during fast charging of Li-ion batteries¹⁹. Janek's group published a series of papers investigating the impedance of Li metal in cells employing solid-state electrolytes with GEIS²⁰. Among other things, the growth kinetics of lithium metal on different model electrodes were investigated, revealing complex heterogeneous electrodeposition behavior and morphological aspects²¹. The performance of Li metal and Li-Mg metal alloy anodes was also compared and investigated. Alloying lithium with 10 at. % of magnesium effectively prevented the formation of macroscopic pores, but the Li-Mg alloy exhibited kinetic limitations due to the chemical diffusion of lithium in the alloy²².

Despite the successful application of GEIS in many battery systems, it is extremely important to emphasize that during such measurements the system changes to some extent due to the DC bias, which can lead to a (significant) distortion of the measured impedance. To minimize this, the measurement time can be shortened. In this case, however, the low-frequency part of the battery spectrum (e.g. below 1 Hz–0.1 Hz) is usually not accessible, as the measurement takes a very long time (in the order of tens of minutes or even several hours). Recently, however, it has been shown that the omission of the low-frequency part means that one cannot obtain information on several critical battery processes such as the diffusion of active species in the porous electrode, in the separator, as well as in active insertion particles^{6,23,24}. In principle, a way of circumventing this shortcoming could be through the use of multisine perturbation^{25–29}, however, we have not employed this approach in this study.

Results and discussion

Here we propose an upgrade of the conventional dynamic impedance measurement method for use in battery research as well as in other electrochemical fields, where the DC bias leads to significant temporal variations of the system during the measurement. The first essential element of the proposed *operando* EIS is the use of a three-electrode cell instead of the predominantly used two-electrode coin or pouch laboratory cell. The second essential element of this technique is the combination of information from the measured EIS spectrum and the overvoltage from the underlying galvanostatic charge or discharge curve. Finally, as shown in this work, the use of the present *operando* EIS method only makes sense when combined with all steps of the measurement under OCV conditions (i.e. steps a–e), as highlighted in Fig. 1.

We demonstrate the advantages of the proposed *operando* EIS using the example of a Li-metal electrode that is subjected to repetitive stripping and plating, which is known to lead to the formation of complex interface structures^{30–33}. The measuring cell is shown schematically in Fig. S2. A crucial element of the analysis is the use of a stable reference electrode. In our case, this was a lithiated gold micro-reference electrode, the stability of which has been demonstrated previously³⁴. In the case of the present symmetric cells, a stable reference electrode provides the crucial information about the different behavior of the two electrodes during each half-cycle, as will be shown in continuation.

Before we apply the *operando* EIS to the lithium-metal system, we first explain the typical results of a galvanostatic cycling experiment on a conventional two electrode symmetrical Li||Li cell cycled with 1M LiTFSI in TEGDME:DOL 1:1 (v:v) electrolyte (Fig. 2). During the first half cycle (Fig. 2b–d), lithium is stripped from the counter electrode and deposited on the working electrode. Since lithium metal passivates under the given circumstances, part of the electrodeposited lithium is lost during the reactions with the electrolyte and forms the SEI layer (Solid Electrolyte Interphase). During the charging process, this

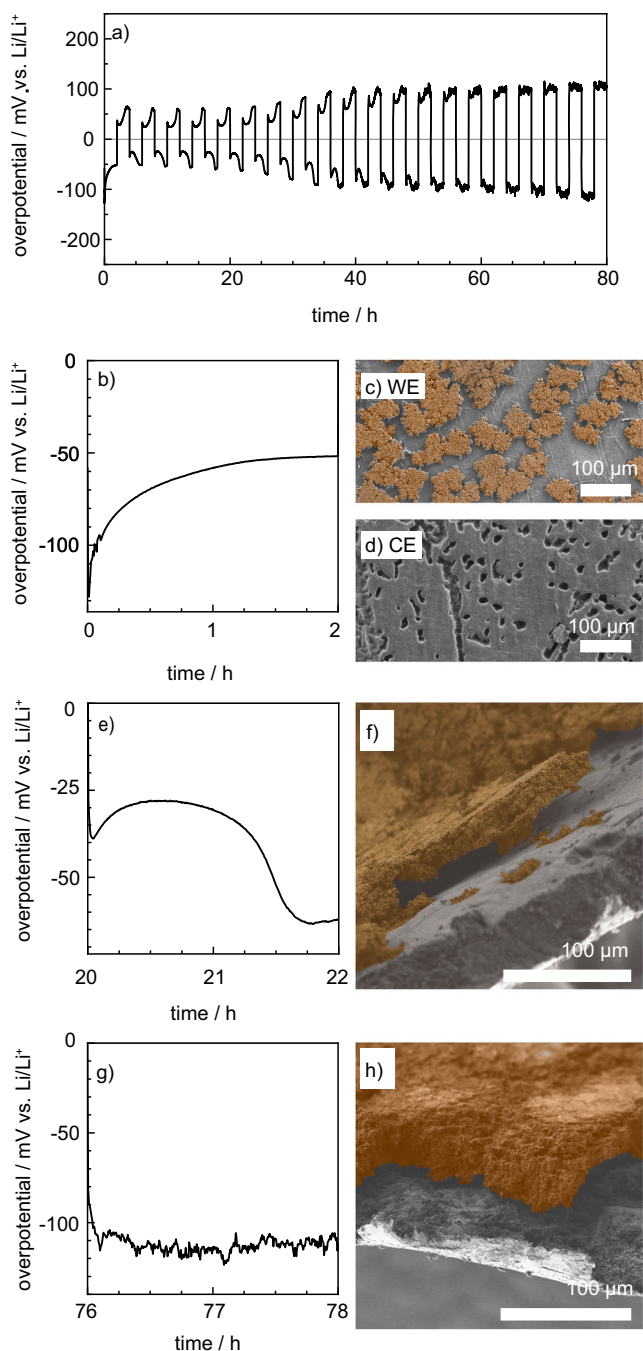


Fig. 2 | Galvanostatic experiment involving Li metal stripping and plating showing three different typical half cycle overpotential variations and corresponding morphologies. **a** Overall potential change with time for Li metal stripping and plating experiment using 1 M LiTFSI in TEGDME:DOL 1:1 (v:v) electrolyte and 0.5 mA/cm² current density. **b** 1st half-cycle overpotential. **c** SEM micrograph of the working electrode (undergoing plating) after the 1st half-cycle in **(b)** with Li deposits colored brown. **d** SEM micrograph of the counter electrode (undergoing stripping) after the 1st half cycle in **(b)**. **e** The negative part of the 5th cycle of the stripping and plating experiment. **f** Morphology of the lithium electrode after the 5th cycle of operation with Li deposits colored in brown. **g** The negative part of the 20th cycle of the stripping and plating experiment. **h** Morphology of the lithium electrode after the 20th cycle of operation with Li deposits colored brown.

deposited lithium is stripped off and deposited back onto the counter electrode. The duration of charging and discharging remains the same because both electrodes have a large excess of lithium metal compared to the amount we strip and deposit. When we reach the limit of

lithium metal that has been deposited during discharge and has been lost to some extent due to side reactions, further stripping is possible by pitting from the bulk lithium metal electrode [1].

Due to the multiple effects described above, this basic experiment already shows different types of variations in the overpotential, depending on the particular cycle of utilization. In the first half cycle, the cell's overpotential decreases sharply and stabilizes at about half of the initial overpotential value (Fig. 2b). In later cycles, the variation of the overpotential is more complex, with an initial peak and decrease and a later increase in values (Fig. 2e). Towards the end of the experiment, the overpotential of a single half-cycle shows a lower absolute variance, but the signal appears to be erratic—it contains noise of the order of 5 mV (Fig. 2g). Ex situ analysis of the Li electrodes shows that about 60% of the surface of the working electrode is covered with islands of high-surface-area Li deposits after the first half cycle (Fig. 2c), while the counter electrode exhibits changes due to pitting that affect an estimated 10% of the electrode surface (Fig. 2d). The morphology of the electrodes in later cycles is more uniform with complete coverage of the electrode deposits. The total thickness of the deposits determined varies from 30 μm after 5 cycles (Fig. 2f) to more than double that after 20 cycles of cell operation (Fig. 2h).

Although the basic galvanostatic electrochemical experiment, especially in combination with additional information from imaging techniques, provides important initial information about the processes that occur in Li electrodes during cycling, such data are difficult to quantify and break down into fundamental (elementary) processes. Examples of such elementary processes expected from general models for porous interfacial structures have been identified in our previous work³: (i) migration of species through the bulk electrolyte contained in the porous separator, (ii) migration of species through the electrolyte in the pores of the porous part of the SEI, (iii) migration of Li⁺ ions through the compact part of the SEI (complicated in the case of dendritic growth due to the formation of a dendritic layer of live Li metal, which creates a virtually porous Li electrode with a large surface area), (iv) charge transfer reaction at the interface between the solid Li metal and the SEI layer, (v) diffusion through the porous layer of the SEI, (vi) diffusion through the live dendritic Li metal layer formed on the electrode surface, (vii) diffusion through the passivation layer of the remaining high surface area deposits formed on the electrode surface, (viii) diffusion through the porous separator.

At least some of the elementary processes listed above can be identified and quantified with the proposed *operando* EIS, as will be shown in the continuation.

Analysis of first half cycle with *operando* EIS

Operando EIS was initially applied to the first half cycle of Li metal stripping and plating using LP40 electrolyte. The contributions of the working and counter electrodes were determined separately by using a microreference electrode, whose reliability was first investigated by comparing two and three-electrode (2E and 3E) experiments (Supplementary Note 4). The calibration of the cell setup was conducted through EIS measurements of glassy carbon electrodes in 2E and 3E configuration (Supplementary Note 5). In addition, the potential fluctuations during *operando* EIS measurements were determined to evaluate the drift and stability of the EIS measurements (Supplementary Note 6).

The impedance spectra measured during the first half cycle of stripping and plating on Li electrodes are shown in Fig. 3 (in black) as stacked Nyquist plots tilted by 90°. The plots are drawn so that their low-frequency points correspond exactly to the overpotential measured at the same time as the impedance spectrum (drawn in red). The axis corresponding to the imaginary part of the impedance (top) has the same unit as the axis for the real part of the impedance (right). At the same time, the scale for the overpotential (left) is directly correlated with the axis for the real part of the impedance (right) when the

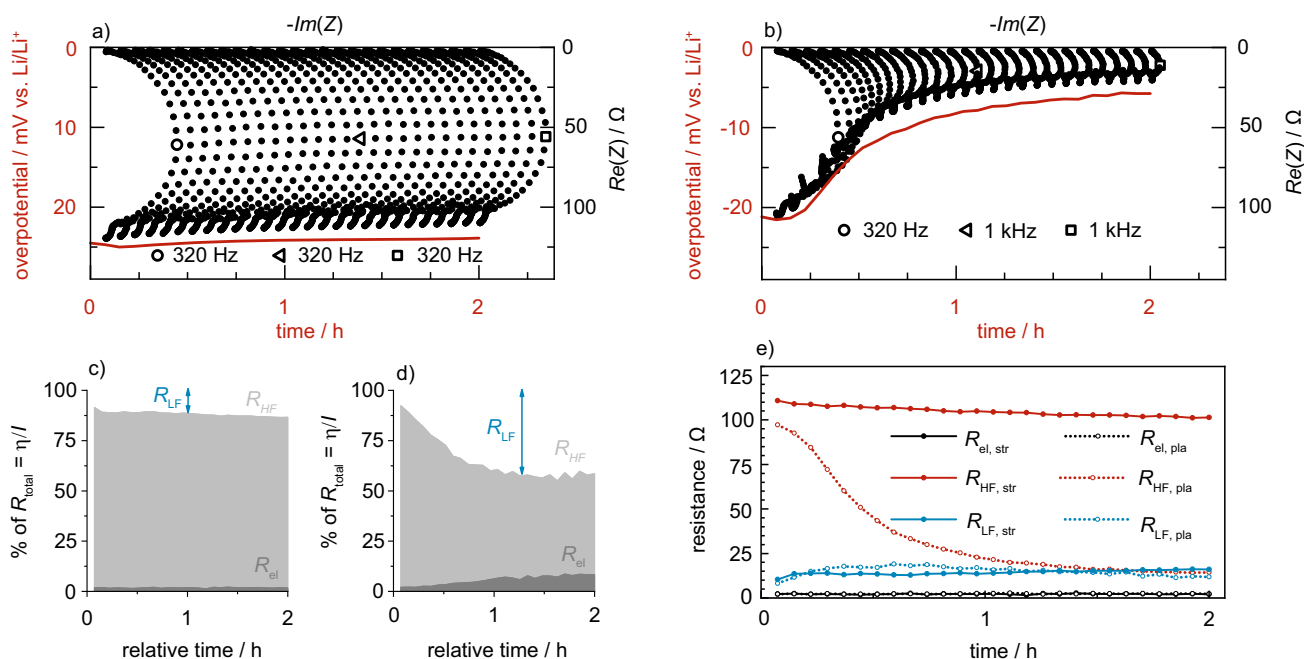


Fig. 3 | Operando impedance spectroscopy experiment during the first half cycle of Li metal stripping and plating on Li || μ Au || Li three-electrode cell.

a Operando EIS spectra (black points, scale on top and right) and overpotential (red curve, scale on bottom and left) during stripping with LP40 electrolyte and 0.1 mA/ cm^2 current density. Symbols mark peak frequencies of the 1st, 14th and 27th spectrum and **(b)** plating during the same half cycle as in **a**). The red curves correspond directly to the values in Fig. S3e. The first value of the red curve is the overpotential value that was measured simultaneously with the first (high) frequency point (1 MHz) in the first impedance spectrum. The subsequent overpotential values were measured together with the last (low) frequency points (20 mHz) in the measured spectra. **c, d** The

percentage contribution of R_{el} (dark grey area), R_{HF} (light grey area), and R_{LF} (white area, marked with blue arrow) resistance to the total resistance for stripping and plating, respectively. **e** Evolution over time of the electrolyte resistance (black lines), the high frequency arc resistance (red lines) and the low frequency resistance (blue lines) contributions for the whole cell. Contributions for the electrode undergoing stripping are plotted in full lines and dots, contributions for the electrode undergoing plating are plotted in dotted lines and open circles. Note that the noise visible in **d**) is due to the instability of the E_{CE} potential measurement during the three-electrode operando impedance experiment.

DC current amplitude is considered. The more traditional representations of the data in the form of Nyquist and Bode plots can be found in Figs. S6 and S7. To demonstrate the quality of the EIS measurements, we have conducted Kramers-Kronig analysis of one of the spectra from the stripped electrode and two spectra from the plated electrode (Fig. S8).

The difference between the total resistance, $R_t = \eta/I$ (red curve in Fig. 3a, b), where I is the applied current and η is the measured overpotential, and the lowest frequency data point for each spectrum (i.e. the maximum impedance from the EIS) is between 4 and 9.5 Ω for the stripped electrode (Fig. 3a) and 4 and 23 Ω for the plated electrode (Fig. 3b). We note that the results of Fig. 3a in particular show very good agreement between the two techniques, confirming that the measurements very likely fulfil the conditions of linearity. The possible reasons for the small differences are as discussed in Supplementary Note 8. To further evaluate the data shown in Fig. 3a and b, we processed the spectra in Zview (Supplementary Note 9) to obtain the value of the resistive intercept (electrolyte resistance, R_{el}), the magnitude of the high-frequency impedance arc (R_{HF}) and the low frequency impedance contributions (R_{LF}). The values of these three parameters as a function of cycling time are shown in Fig. 3c–e.

During stripping, only very small changes are observed in the first half cycle of the experiment (Fig. 3a), which is reflected in almost constant values of the corresponding parameters with stripping time (Fig. 3c and solid lines in Fig. 3e). In contrast, the changes in the parameters are much more pronounced for the electrode that was plated (Fig. 3d and dashed lines in Fig. 3e). Importantly, the shape of the EIS spectrum changes from a relatively symmetrical arc to an arc with an angle of 45° in the high frequency range. Such a shape is

attributed to transport through the porous structure of the electrode^{3,5} (Figs. 3b and S6b). This is confirmed by ex situ analysis of the cell (Supplementary Note 10). The R_{el} and R_{LF} values and trends are similar to the electrode subjected to stripping.

By comparing the temporal evolution of the different parameters defined above (Fig. 3e), one can easily evaluate the contribution of each process to the overall overpotential of the cell. During the entire stripping half-cycle, the process that can be seen as a high-frequency arc contributes by far the most to the overall overpotential of the cell. Conversely, the size of the high-frequency arc decreases significantly over time during plating, which is due to the increase in the surface area of the plated metallic structures. This change can be used to estimate the increase in surface area of the active electrode, which was found to be about 60-fold (Supplementary Note 11).

Repeatability of the experiments is shown in Fig. S18, where the overpotential and EIS spectra of the electrode undergoing stripping or plating is compared. As evident, the largest differences in between repetitions are in the overpotential of the stripped electrode, which is directly related to the SEI resistance of the electrode. Since the Li metal foil was not pretreated before cell assembly, the variation is attributed to inhomogeneity of the native SEI layer. For the employed current density and electrolyte, the relative decrease of the SEI arc in stripping was for a factor of 1.09 ± 0.06 , while for plating, the high frequency arc decreased for $86 \pm 2\%$.

Analyzing the results in Fig. 3, one might conclude that similar (or even more accurate) results would be obtained using the conventional EIS technique of Fig. 1a, i.e. by interrupting the discharge at pre-selected times and measuring the corresponding EIS spectra after equilibration of the cell at the corresponding OCV conditions

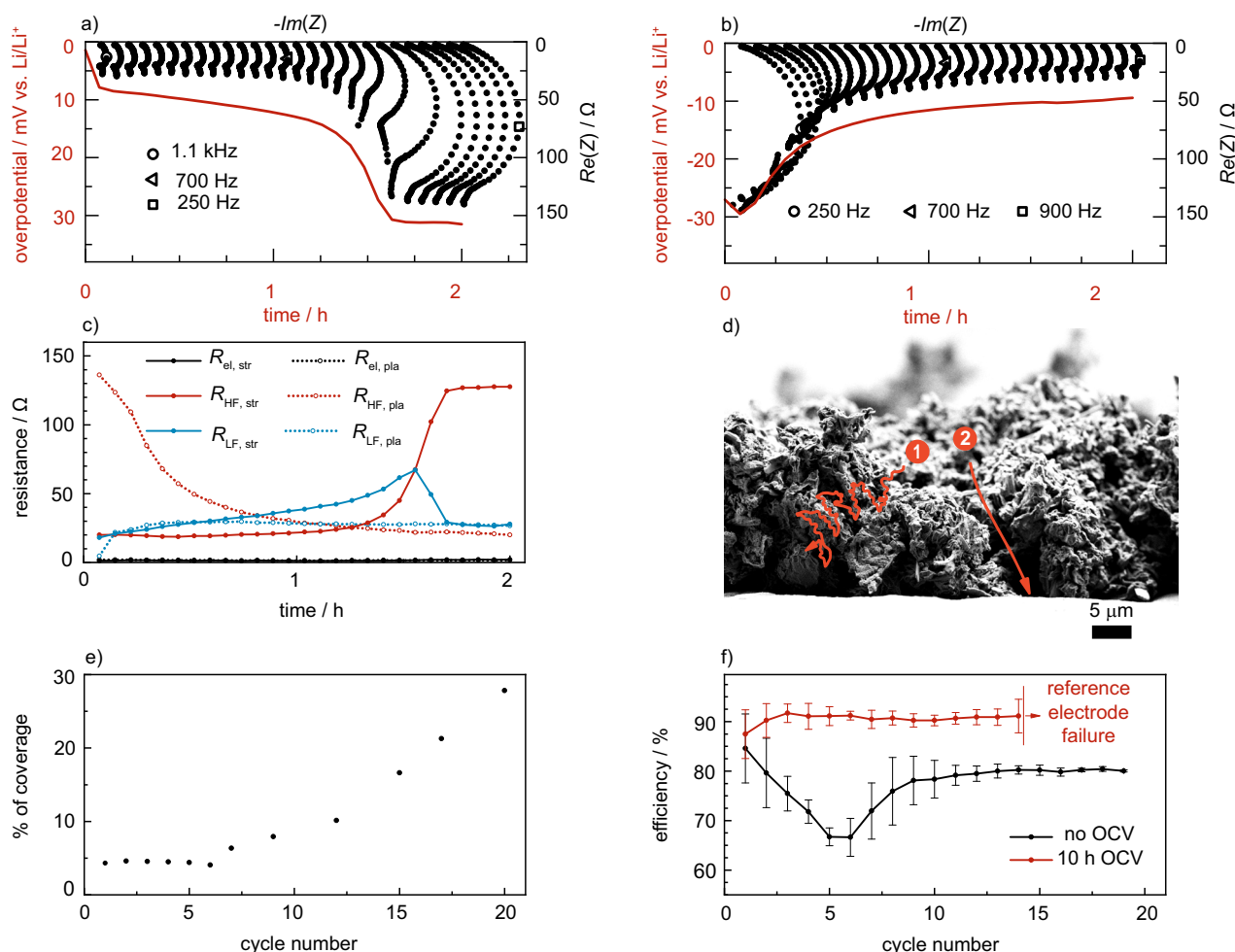


Fig. 4 | Operando impedance spectroscopy experiment during the 20th cycle of Li metal stripping and plating on Li||μAu||Li three-electrode cell. **a** Operando EIS spectra (black points, scale on top and right) and overpotential (red curve, scale on bottom and left) during stripping with LP40 electrolyte and 0.1 mA/cm² current density. Symbols mark peak frequencies of the 1st, 14th and 27th spectrum and **(b)** plating during the same half cycle as in **a**). The red curves show the overpotential values and correspond directly to values in Fig. S3f. **c** Time evolution of the electrolyte resistance (black line) and the contributions of the high-frequency arc resistance (red line) and R_{LF} (blue line) for the entire cell. Contributions for the electrode undergoing stripping are plotted in full lines and dots, contributions for

the electrode undergoing plating are plotted in dotted lines and open circles. **d** Scheme of the various transport pathways to the available lithium. Path 1 shows tortuous pathway in porous lithium deposits. Path 2 shows less tortuous, direct, pathway to the bulk electrode. **e** The percentage of surface coverage with deposited lithium on Li-metal electrodes changes with the number of cycles of stripping and plating. **f** Change in stripping efficiency from previously deposited Li on Li-metal electrode with and without 10 h OCV periods after plating. Error bars show standard deviation in stripping efficiency for each cycle number between four measurements.

(EIS@OCV). However, Fig. S19 (Supplementary Note 12) shows that the spectra measured with EIS@OCV differ significantly from the present spectra measured with *operando* EIS. For example, the difference in the magnitude of the low-frequency arc is one order of magnitude, while the difference in the peak frequency of this arc is even two orders of magnitude. This clearly underlines the general need to perform *operando* EIS in addition to EIS@OCV measurements if we want to better understand the nature of the processes that take place during battery operation.

Subsequent half cycles

In the following cycles of Li metal stripping and plating with LP40 electrolyte, the trends in overpotential and impedance spectra become more complex. As an example, the *operando* impedance data for the 20th cycle are shown in Fig. 4 (the corresponding Nyquist and Bode plots can be found in Figs. S21 and S22). The trends for the electrode being plated (Fig. 4b) are similar to those observed in the first half cycle (Fig. 3b). However, the trends for the electrode that is stripped (Fig. 4a) differ significantly from those observed in the first

half cycle (Fig. 3a). The increase in overpotential in the first part of the later half-cycles has been attributed to the gradual consumption of accessible lithium from the high surface area lithium deposits. When this relatively easily accessible Li metal is completely consumed, pitting begins to occur from the bulk of the flat electrode, which can be seen as the plateau of the overpotential in the second part of the half-cycle^{30,31,35}.

The impedance data of the present *operando* EIS technique support the previously formulated hypothesis in the literature, which was based solely on the overvoltage trend. In the first part (i.e., until about 1 h) of the half-cycle in Fig. 4a, it can be seen that the high frequency contribution remains almost stable, while the difference between the overpotential value and value and the resistance of the lowest measured frequency point increases, indicating an increase in the various diffusion impedances taking place in this system. In the second part of the half cycle (after about 1 h), the high frequency arc also starts to increase in magnitude, indicating a reduced size of the active surface and the beginning of pitting on the bulk Li metal electrode³⁰. The time at which this occurs probably depends on the degree of passivation of

the high surface area lithium deposits. With low passivation, the increase in overpotential occurs at later stages of the half-cycle, whereas a higher degree of passivation would mean that pitting of the bulk electrode begins very soon after the start of the half-cycle.

Similar to the results of the first half-cycle, we fit the spectra with a simplified equivalent circuit (Fig. S12) and show the results in Fig. 4c. As mentioned above, the results for the electrode that is plated are very similar to those of the first half-cycle, as are the trends for R_{HF} and R_{LF} . For the electrode that is stripped, the trend is different. Within the first hour, the R_{HF} (the size of the HF arc) remains more or less constant, i.e. it does not follow the increasing trend of the overpotential (red line in Fig. 4a). This means that the R_{LF} increases during this period, which we attribute to an increase in the diffusion distances required to reach the increasingly hidden Li metal in the high surface area deposits. However, as soon as the R_{HF} increases, the R_{LF} starts to decrease. This could be explained by the scheme in Fig. 4d. In the first part of the half-cycle, stripping takes place in the high surface area deposits. The further this process progresses, the more difficult it becomes to reach the lithium metal, as the path to the remaining deposits is long, tortuous and in increasingly narrow pores (pathway 1). After the Li available in the large surface area deposits is used up, pitting begins in the bulk of the electrode, which means that the transport path is shorter, less tortuous and probably through pores with larger dimensions (pathway 2).

The results of the *operando* EIS measurements shown above are consistent with ex situ analysis of the cell, which shows extensive lithium deposits with a large surface area growing through the glass fiber separator (Fig. S23). We also observed that the morphology of the tip of the reference electrode exhibits a blooming feature, which we attribute to the process of lithiation of the gold wire, as a similar morphology was observed in the reference electrode of a cell where only half a cycle of stripping/plating was performed (Fig. S24).

The complete data for the values of R_{el} , R_{HF} and R_{LF} for the stripping and plating half-cycles between the 2nd and 20th cycle are shown in Fig. S25. If we focus mainly on the trends observed for R_{LF} , we see that R_{LF} shows different types of variations as the number of cycles increases. In the initial cycles, the maximum RLF value occurs at longer intervals (between 1 and 2 hours). As the cycling progresses, this peak shifts to less than 1 hour by the 4th or 5th cycle, after which it gradually increases again until stabilizing (Fig. S25f). It can be shown that this value is close to the Coulombic efficiency determined for a Li||Cu cell with the same electrolyte (Fig. S26). Interestingly, the initial cycles in the Li||Cu cell experiment show a similar variation of Coulombic efficiency values in the initial cycles as for the Li||Li cells. Since we relate this point of maximum to the degree of passivation of the electrode (Fig. 4), we performed additional experiments to understand why this point shifts during cycling. Using SEM and optical microscopy (Figs. S27–29), we show that the coverage of the electrodes appears to be almost constant in the first cycles.

The results shown above strongly suggest that during the first few cycles of stripping and plating with the electrolyte and current density used, the lithium deposits in exactly the same locations (probably the defective areas in the SEI) of the original electrode. As the material is always deposited in the same location in dendritic form, an increasingly complex morphology of the deposits forms and the transport impedance increases. The phenomena during deposition are mirrored during stripping, as the extraction of Li from an increasingly tortuous and closed-pore network of deposits again exhibits transport difficulties. This essentially means that the increase in overpotential due to the onset of Li pitting is not due to the depletion of Li reserves in the large-scale deposits, but rather to the remaining Li being too difficult to access.

To test this hypothesis, we inserted OCV periods between each half-cycle of stripping/plating. If the point of R_{HF} rise depends on transport difficulty rather than the degree of passivation of the lithium deposits, increasing the time between plating and stripping would

increase the efficiency of stripping and shift the point of R_{HF} rise to longer half-cycle times. Interestingly, the point of overpotential rise did not change significantly when 30 min or even 3 h OCV periods were inserted between each stripping/plating half-cycle (Fig. S29), suggesting that the mass transport limitations likely occur within the narrowest pores (e.g., in the porous part of the SEI). This also implies that most of the passivation occurs rapidly after the deposition of Li on a large surface area. The amount of Li metal consumed in the passivation processes over the longer test period is negligible and the Coulombic efficiency does not decrease. On the other hand, when 10-hour OCV periods were included between stripping and plating, the cell did not exhibit a minimum in stripping efficiency and also showed an increase in overall efficiency to 90% in later cycles (Fig. 4f). The lithium metal is therefore still available in the deposits with a large surface area and can be utilized if sufficiently long rest periods are included. If the diffusion fronts cannot relax, bulk pitting is preferred to stripping from the remaining reserves, which is difficult to achieve.

We have found reports where introduction of rest periods during Li metal stripping and plating decreases the cycling efficiency^{36,37}. There is nevertheless a large difference between determination of Coulombic efficiency of Li metal stripping and plating using Li||Cu vs. Li||Li cells as done in this study. When Li metal is plated on copper substrates it can dissolve from the support due to the mixed potential of the two metals with copper acting as the nobler metal³⁸.

Occurrence of soft short circuits

In the half-cycles towards the end of the experiment, the overpotential remains of a similar magnitude as in the first cycles (100 mV). The overall fluctuation of the signal is smaller—after the initial increase, the overpotential fluctuates by only about 15%. However, the signal is more irregular and exhibits a strong noise at an amplitude of 5 mV. This type of signal is thought to be caused by Li metal dendrites growing through the separator and coming into contact with the other electrode, a phenomenon that has already been described for zinc metal electrodes⁹. These dendrites lead to an internal short circuit, but the contact does not last long, either by passivation of the dendrites or by deformation due to heat generation.

Operando EIS spectra measured on two-electrode symmetrical Li||Li cells using 1M LiTFSI in TEGDME:DOL 1:1 (v:v) electrolyte (Fig. S30) show noise in the low frequency range, while the high frequency arc is repeatable with an approximate resistance size of 125–150 Ωcm^2 and 30 kHz peak frequency. The total resistance calculated from the overpotential values agrees very well with the resistance determined from the impedance measurements (Fig. S31). The very high characteristic peak frequency is the parameter that prompted us to investigate the origin of the impedance contribution in more detail, since a typical peak frequency of a high-frequency impedance arc in Li||Li symmetrical cells of similar resistance size is typically at least one order of magnitude lower²³. When EIS spectra are measured at OCV after the *operando* impedance spectroscopy experiment is completed, the resistance of the high-frequency arc increases, while its characteristic peak frequency decreases (Figs. 5a and S32).

Morphological analysis of the electrodes and Celgard 2320 separator harvested from the cell after the *operando* and EIS@OCV measurements revealed extensive growth of high surface area lithium (Fig. 5b) on the electrode surface. Some of these deposits were transferred to the surface of the separator when the cell was disassembled (Fig. S33). Apart from the Li metal deposits, the separator also exhibited a thin layer coverage below the Li metal deposits, which we attribute to the transfer of the SEI layer from the electrode. FIB-SEM preparation and analysis of the cross-section of the separator showed the growth of the Li metal through the pores of the separator, as shown in Figs. 5c and S34.

To explain the characteristics of the impedance spectra observed in *operando* and EIS@OCV measurements, a transmission

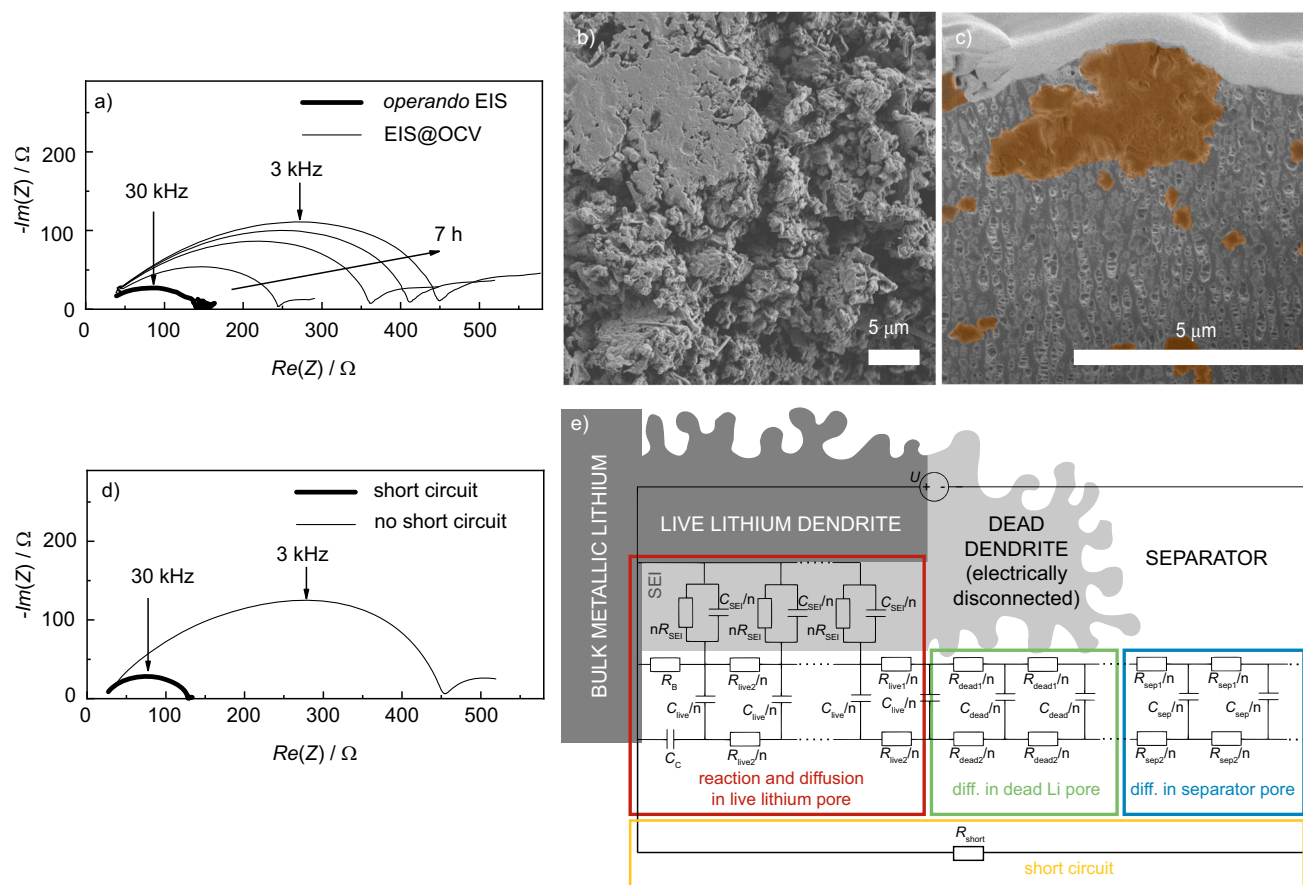


Fig. 5 | Measured and simulated impedance spectra and morphological analysis of the cell with indications of short circuit formation. **a** Nyquist plots for impedance spectra of the Li || Li two-electrode cell with 1M LiTFSI in TEGDME:DOL electrolyte and Celgard 2320 separator: the spectrum in bold was the last spectrum measured operando (25 cycles of stripping and plating at 0.5 mA/cm² to 1 mAh/cm²), thin lines show EIS@OCV measurements after the end of the galvanostatic experiment and 15 minutes of relaxation. The time course shows the changes over a period of 7 hours. **b** Surface morphology of the Li metal electrode harvested from the cell after the experiment in **a**. **c** Cross section of the Celgard separator from the cell in **a** with pronounced Li metal dendrite growth through

the separator pores coloured in brown. **d** Transmission line model simulation of impedance spectra with (thick black line) and without short circuit (thin black line) using the circuit in **e**. **e** Scheme of the transmission line model of a Li metal electrode with high surface area Li metal deposits on the surface and a short circuit due to dendrites penetrating the separator (yellow). Transport of active (all resistors indexed with 1) and inactive (all resistors indexed with 2) species in the separator (blue region), completely passivated lithium deposits (green region) and lithium deposits acting as porous electrode (red region) is considered.

line model was proposed (Fig. 5d, Supplementary Note 14). The upper part of the circuit corresponds to the previously published model of a Li metal electrode with high-surface-area porous deposit(s) on its surface³. To describe the internal short circuit, an additional parallel element (Fig. 5d, R_{short} , in yellow) was inserted. The TLM was used to simulate the impedance spectra with and without the short circuit (Fig. 5e). It can be seen that the changes in shape, size and typical frequencies are reproduced very well when a typical impedance spectrum of a well-functioning cell (black spectrum) is short-circuited with a simple resistive element (orange spectrum), which in this case had a value of 18 Ω. If we take the value for the resistivity of lithium metal at room temperature ($9.5 \times 10^{-8} \Omega \text{m}$ ³⁹) and the distance between the Li electrodes (20 μm), we can obtain an estimate for the average cross-sectional area of the dendrites causing the short circuit of around 0.1 μm². In a dynamic experiment with constant current flow, it is of course to be expected that the cross-sectional area of the short-circuited dendrites changes over time—hence the noise in typical measurements with a short circuit. The good agreement between the experimental impedance spectra (Fig. 5a) and the modelled spectra (Fig. 5e) is further proof that the results of the *operando* EIS can be meaningfully analyzed with state-of-the-art modelling tools.

To summarize, we have demonstrated the powerful capabilities of the *operando* EIS technique using the example of a battery cell with two lithium metal electrodes. Unlike previous methods that primarily rely on electrochemical impedance measurements under DC current or potential bias, our approach integrates dynamic impedance data with real-time overvoltage analysis during galvanostatic charge/discharge cycles. This combination provides a deeper and more nuanced understanding of battery behavior, especially when performed under linear conditions. The use of a stable reference electrode is crucial in isolating and analyzing the distinct responses of the working and counter electrodes. Finally, the proposed method also includes measurements under steady-state conditions (OCV) and modeling of the measured spectra using physics-based models (in our case physics-based transmission lines). We show that such a combination of several electrochemical approaches can be used to test the validity of selected existing hypotheses in the literature and, more importantly, to discover new phenomena. Further improvements to the shortcomings of the approach could be possible through the employment of multisine excitation signal. While the focus of this study was on lithium batteries, the versatility of *operando* EIS makes it applicable to a wide range of electrochemical systems with complex transport and reaction mechanisms.

Methods

Materials

All handling of materials was conducted inside an argon-filled MBraun glovebox where the O₂ and H₂O levels were kept below 1 ppm. Lithium metal ribbon (FMC, 110 µm) was cut into 2 cm² electrodes and used without any pre-preparation. Commercial LP40 electrolyte (1 M LiPF₆ in EC:DEC 1:1 (v:v), Elyte innovations) was used as received. 1 M LiTFSI in TEGDME:DOL 1:1 (v:v) electrolyte was prepared in the laboratory out of previously dried materials: lithium bis(trifluoromethanesulfonyl) imide (LiTFSI, Sigma Aldrich, 99%) was dried at 140 °C in vacuum overnight, tetraethylene glycol dimethyl ether (TEGDME, Sigma-Aldrich, 99%) and 1,3-dioxolane (DOL, Thermo Scientific, 99.5%) solvents were dried in a multistep process. First, they were pre-dried using molecular sieves (4 Å, ASGE, beads) and then dried with a K/Na alloy (wt. ratio 3/1) overnight by stirring at reflux temperature, and finally distilled at normal pressure, transferred into a flask (at 200 °C overnight for DOL and 5 mbar, 150 °C for TEGDME) with good sealing, and stored. The final water content was below 5 ppm. The electrolyte was prepared by weighing the calculated amount in a volumetric flask and filled to the marked line using 1:1 (v:v) mixture of solvents. Celgard 2320 and GF-A glass fiber (Whatman, 260 µm) separators were dried at 50 °C in vacuum for a few days before transferring them to the glovebox. Cells were assembled by stacking the electrodes and separator and wetting the separator with the stated amount of electrolyte. If not stated otherwise, 100 µL of electrolyte was used for 20 mm diameter glass fibre separators and 20 µL for Celgard 2320. The cell was then sealed in a pre-manufactured and pre-dried triplex foil (PE 90 µm/Al 10 µm/PET 20 µm) casing with two Ni contacts. Gold microwire (Good-fellow, 50 µm thickness, 0.7 µm polyimide insulation) was lithiated and used as a reference electrode. More details on the design of the three-electrode cell are available in Supplementary Note 3. Calibration of the cell setup was performed by exchanging the Li electrodes with glassy carbon discs (HTW, Germany, 2 cm²). Carbon felt interlayer H14 (Freudenberg) was employed in some cells (Supplementary Note 12) and placed between the Li counter electrode and separator.

Electrochemical testing

Electrochemical testing on the cells was conducted on VMP3 Bio-logic potentiostats/galvanostats with the cells placed inside Binder temperature chamber kept at 25 °C. The cell was placed in a Faraday cage by placing it in a plastic bag surrounded with Ni foil, which was connected to the potentiostat/galvanostat's channel ground. Stripping and plating tests were conducted at various current densities as specified with each figure. Electrochemical impedance spectra measured at open circuit potential were measured with a rms amplitude of 10 mV and in the range of 1 MHz–20 MHz or 1 MHz–1 mHz (as specified with each measurement). Dynamic impedance measurements were conducted with a direct current density of 0.1 mA/cm² and alternating current amplitude of 20 µA/cm². 27 spectra repetitions were measured in a single half cycle with the frequency range of 1 MHz to 20 mHz.

Ex situ analysis

After the electrochemical tests, some cells were disassembled in the glovebox and the electrodes were removed for further chemical and morphological analyzing. For this purpose, the electrodes were washed with DOL to remove residues of electrolyte salts. Scanning electron microscopy measurements were performed with a field emission scanning electron microscope (FE SEM) Supra 35VP from Zeiss, Germany. The samples were placed in the SEM on a custom-made holder, which was vacuumed in the glovebox and opened when vacuum was reached in the SEM. Microscopic images were usually taken using an electron gun with an accelerating voltage of 1 kV, a low setting due to the instability of the materials under the electron beam. Lithium deposits and dendrites were colored brown using Adobe Photoshop.

Specimens intended for FIB cross-section analysis were transferred to the FIB chamber with a vacuum transfer interlock ALTO 1000 (Gatan, US) without exposure to air at any time during the procedure. Sample cross-sections were analyzed using the FIB-SEM Helios Nanolab 650i (FEI, U.S.A.) equipped with a Pt gas injection system and the X-MAX 50 energy dispersive spectrometer (Oxford, UK). Due to the high sensitivity of the sample to the ion beam, the surface was first protected with a 300 nm in situ deposited Pt film induced by an electron beam (2 kV @ 0.4 nA). Additional platinum was deposited in situ on the first layer with a Ga⁺ ion beam (30 kV @ 0.23 nA) to obtain a Pt surface protection layer with a final thickness of 800 nm. The cross sections were prepared with focused Ga⁺ ions at 30 kV @ 2.5 nA and with sequentially reduced currents down to 80 pA for the case of the final ion polishing step. Morphological images of the surface and cross sections were acquired with a low energy electron beam (2 kV @ 50 pA) and a standard ETD detector. Detailed information and phase contrast images of cross sections were acquired using InColumn integrated SE/BSE detectors and a pre-monochromated electron beam at 1 kV energy and 25 pA beam current.

Optical microscopy imaging intended for determination of coverage with deposits were conducted inside the glovebox using SMART microscope ALL-IN-ONE 1080p. The images were processed in ImageJ 1.54 g software to determine the degree of coverage using Analyze Particles option with Renyi Entropy thresholding method.

EIS spectra processing and simulations

Kramers-Kronig (KK) analysis of operando (dynamic) impedance measurements was carried out using the online software Lin-KK developed by Karlsruhe Institute of Technology (KIT), Germany (<https://www.iam.kit.edu/et/english/Lin-KK.php>). Examples of the KK analysis are shown in Supplementary Note 7.

Some EIS spectra were fitted in Zview using the method and equivalent circuit as specified in Supplementary Note 9. Zview version 4.0b was used.

The impedance spectra of short-circuited Li-Li symmetrical cells were modelled using a previously reported transmission line model (see ref. 4) to which an additional resistor was added. The details of the model are explained in Supplementary Note 14.

Data availability

Raw and processed data generated in this study is available at <https://doi.org/10.5281/zenodo.14800073>⁴⁰.

References

- Barsoukov, E. & Macdonald, J. R. *Impedance Spectroscopy Theory, Experiment, and Applications*. (Wiley & Sons, Inc., 2005).
- Gaberšček, M. Understanding Li-based battery materials via electrochemical impedance spectroscopy. *Nat. Commun.* **12**, 6513 (2021).
- Wang, S. et al. Electrochemical impedance spectroscopy. *Nat. Rev. Methods Prim.* **1**, 41 (2021).
- Drvarič Talian, S., Moškon, J., Dominko, R. & Gaberšček, M. Reactivity and Diffusivity of Li Polysulfides: A Fundamental Study Using Impedance Spectroscopy. *ACS Appl Mater. Interfaces* **9**, 29760–29770 (2017).
- Drvarič Talian, S., Moškon, J., Dominko, R. & Gaberšček, M. Impedance response of porous carbon cathodes in polysulfide redox system. *Electrochim. Acta* **302**, 169–179 (2019).
- Moškon, J., Žuntar, J., Drvarič Talian, S., Dominko, R. & Gaberšček, M. A Powerful Transmission Line Model for Analysis of Impedance of Insertion Battery Cells: A Case Study on the NMC-Li System. *J. Electrochem Soc.* **167**, 140539 (2020).
- Walusiński, S., Barchasz, C., Bouchet, R. & Alloin, F. Electrochemical impedance spectroscopy study of lithium–sulfur batteries: Useful

- technique to reveal the Li/S electrochemical mechanism. *Electrochim. Acta* **359**, 136944 (2020).
8. Urquidí-Macdonald, M., Real, S. & Macdonald, D. D. Applications of Kramers–Kronig transforms in the analysis of electrochemical impedance data—III. Stability and linearity. *Electrochim. Acta* **35**, 1559–1566 (1990).
 9. Popkrov, G. S., Barsoukov, E. & Schindler, R. N. Investigation of conducting polymer electrodes by impedance spectroscopy during electropolymerization under galvanostatic conditions. *J. Electroanalytical Chem.* **425**, 209–216 (1997).
 10. Stoyanov, Z., Savova-Stoyanov, B. & Kossev, T. Non-stationary impedance analysis of lead/acid batteries. *J. Power Sources* **30**, 275–285 (1990).
 11. OSAKA, T., MOMMA, T. & TAJIMA, T. In situ Ac Impedance Measurement during Galvanostatic Deposition and Dissolution of Lithium. *Denki Kagaku oyobi Kogyo Butsuri Kagaku* **62**, 350–351 (1994).
 12. Itagaki, M. et al. In situ electrochemical impedance spectroscopy to investigate negative electrode of lithium-ion rechargeable batteries. *J. Power Sources* **135**, 255–261 (2004).
 13. Itagaki, M. et al. LiCoO₂ electrode/electrolyte interface of Li-ion rechargeable batteries investigated by in situ electrochemical impedance spectroscopy. *J. Power Sources* **148**, 78–84 (2005).
 14. Itagaki, M., Honda, K., Hoshi, Y. & Shitanda, I. In-situ EIS to determine impedance spectra of lithium-ion rechargeable batteries during charge and discharge cycle. *J. Electroanalytical Chem.* **737**, 78–84 (2015).
 15. Huang, J., Li, Z. & Zhang, J. Dynamic electrochemical impedance spectroscopy reconstructed from continuous impedance measurement of single frequency during charging/discharging. *J. Power Sources* **273**, 1098–1102 (2015).
 16. Ko, Y., Hwang, C. & Song, H. K. Investigation on silicon alloying kinetics during lithiation by galvanostatic impedance spectroscopy. *J. Power Sources* **315**, 145–151 (2016).
 17. Ratynski, M. et al. A New Technique for In Situ Determination of the Active Surface Area Changes of Li-Ion Battery Electrodes. *Batter Supercaps* **3**, 1028–1039 (2020).
 18. Watanabe, H., Omoto, S., Hoshi, Y., Shitanda, I. & Itagaki, M. Electrochemical impedance analysis on positive electrode in lithium-ion battery with galvanostatic control. *J. Power Sources* **507**, 230258 (2021).
 19. Brown, D. E., McShane, E. J., Konz, Z. M., Knudsen, K. B. & McCloskey, B. D. Detecting onset of lithium plating during fast charging of Li-ion batteries using operando electrochemical impedance spectroscopy. *Cell Rep. Phys. Sci.* **2**, 100589 (2021).
 20. Krauskopf, T., Hartmann, H., Zeier, W. G. & Janek, J. Toward a Fundamental Understanding of the Lithium Metal Anode in Solid-State Batteries - An Electrochemo-Mechanical Study on the Garnet-Type Solid Electrolyte Li_{6.25}Al_{0.25}La₃Zr₂O₁₂. *ACS Appl. Mater. Interfaces* **11**, 14463–14477 (2019).
 21. Krauskopf, T. et al. Lithium-Metal Growth Kinetics on LLZO Garnet-Type Solid Electrolytes. *Joule* **3**, 2030–2049 (2019).
 22. Krauskopf, T., Mogwitz, B., Rosenbach, C., Zeier, W. G. & Janek, J. Diffusion Limitation of Lithium Metal and Li-Mg Alloy Anodes on LLZO Type Solid Electrolytes as a Function of Temperature and Pressure. *Adv. Energy Mater.* **9**, 1902568–1902581 (2019).
 23. Drvarič Talian, S., Bobnar, J., Sinigoj, A. R., Humar, I. & Gaberšček, M. Transmission Line Model for Description of the Impedance Response of Li Electrodes with Dendritic Growth. *J. Phys. Chem. C* **123**, 27997–28007 (2019).
 24. Drvarič Talian, S. et al. Which Process Limits the Operation of a Li-S System? *Chem. Mater.* **31**, 9012–9023 (2019).
 25. Hallemans, N. et al. Operando electrochemical impedance spectroscopy and its application to commercial Li-ion batteries. *J. Power Sources* **547**, 232005 (2022).
 26. Dabiri Havigh, M. et al. Operando odd random phase electrochemical impedance spectroscopy for in situ monitoring of the anodizing process. *Electrochem. Commun.* **137**, 107268 (2022).
 27. Zhu, X. et al. Electrochemical impedance study of commercial LiNi_{0.80}Co_{0.15}Al_{0.05}O₂ electrodes as a function of state of charge and aging. *Electrochim. Acta* **287**, 10–20 (2018).
 28. Dabiri Havigh, M. et al. Operando odd random phase electrochemical impedance spectroscopy (ORP-EIS) for in-situ monitoring of the Zr-based conversion coating growth in the presence of (in) organic additives. *Corros. Sci.* **223**, 111469 (2023).
 29. Dabiri Havigh, M. et al. Application of operando ORP-EIS for the in-situ monitoring of acid anion incorporation during anodizing. *Electrochim. Acta* **493**, 144395 (2024).
 30. Wood, K. N. et al. Dendrites and pits: Untangling the complex behavior of lithium metal anodes through operando video microscopy. *ACS Cent. Sci.* **2**, 790–801 (2016).
 31. Chen, K.-H. et al. Dead lithium: mass transport effects on voltage, capacity, and failure of lithium metal anodes. *J. Mater. Chem. A Mater.* **5**, 11671–11681 (2017).
 32. Bai, P., Li, J., Brushett, F. R. & Bazant, M. Z. Transition of lithium growth mechanisms in liquid electrolytes. *Energy Environ. Sci.* **9**, 3221–3229 (2016).
 33. Tewari, D. & Mukherjee, P. P. Mechanistic understanding of electrochemical plating and stripping of metal electrodes. *J. Mater. Chem. A Mater.* **7**, 4668–4688 (2019).
 34. Solchenbach, S., Pritzl, D., Kong, E. J. Y., Landesfeind, J. & Gasteiger, H. A. A Gold Micro-Reference Electrode for Impedance and Potential Measurements in Lithium Ion Batteries. *J. Electrochem. Soc.* **163**, A2265–A2272 (2016).
 35. Shafiei Sabet, P. & Sauer, D. U. Separation of predominant processes in electrochemical impedance spectra of lithium-ion batteries with nickel-manganese-cobalt cathodes. *J. Power Sources* **425**, 121–129 (2019).
 36. Boyle, D. T. et al. Corrosion of lithium metal anodes during calendar ageing and its microscopic origins. *Nat. Energy* **6**, 487–494 (2021).
 37. Wood, S. M. et al. Predicting Calendar Aging in Lithium Metal Secondary Batteries: The Impacts of Solid Electrolyte Interphase Composition and Stability. *Adv. Energy Mater.* **8**, 1801427 (2018).
 38. Lin, D. et al. Fast galvanic lithium corrosion involving a Kirkendall-type mechanism. *Nat. Chem.* **11**, 382–389 (2019).
 39. Properties of Solids; Electrical Resistivity of Pure Metals. in *CRC Handbook of Chemistry and Physics* (ed. Lide, D. R.) (CRC Press, Boca Raton, Florida, 2003).
 40. Drvarič Talian, S., Kapun, G., Moškon, J., Dominko, R. & Gaberšček, M. Source data for Operando impedance spectroscopy with combined dynamic measurements and overvoltage analysis in lithium metal batteries. *Zenodo* at <https://doi.org/10.5281/zenodo.14800073> (2025).

Acknowledgements

The work was financially supported by Slovenian Research Agency ARIS research project Z2-4465 (S.D.T.) and Slovenian Research Agency ARIS core program funding P2-0393 (M.G.) and P2-0423 (S.D.T., G.K., J.M., R.D.).

Author contributions

S.D.T.: conceptualization, data curation, funding acquisition, investigation, methodology, visualization, writing—original draft preparation, G.K.: investigation, J.M.: writing—review and editing, R.D.: funding acquisition, writing—review and editing, M.G.: writing—review and editing.

Competing interests

The authors declare no competing interests.

Additional information

Supplementary information The online version contains supplementary material available at <https://doi.org/10.1038/s41467-025-57256-0>.

Correspondence and requests for materials should be addressed to Miran Gaberšček.

Peer review information *Nature Communications* thanks Yevgen Barsukov, Sylvain Franger, and the other, anonymous, reviewers for their contribution to the peer review of this work. A peer review file is available.

Reprints and permissions information is available at <http://www.nature.com/reprints>

Publisher's note Springer Nature remains neutral with regard to jurisdictional claims in published maps and institutional affiliations.

Open Access This article is licensed under a Creative Commons Attribution-NonCommercial-NoDerivatives 4.0 International License, which permits any non-commercial use, sharing, distribution and reproduction in any medium or format, as long as you give appropriate credit to the original author(s) and the source, provide a link to the Creative Commons licence, and indicate if you modified the licensed material. You do not have permission under this licence to share adapted material derived from this article or parts of it. The images or other third party material in this article are included in the article's Creative Commons licence, unless indicated otherwise in a credit line to the material. If material is not included in the article's Creative Commons licence and your intended use is not permitted by statutory regulation or exceeds the permitted use, you will need to obtain permission directly from the copyright holder. To view a copy of this licence, visit <http://creativecommons.org/licenses/by-nc-nd/4.0/>.

© The Author(s) 2025